Construction and Building Materials 523 (2026) 146271

Contents lists available at ScienceDirect

Construction and Building Materials

journal homepage: www.elsevier.com/locate/conbuildmat

Understanding the role of fillers in the hydration of citrate-activated BOF slag binder using PARC analysis

S. Yvars [a,*], K. Schollbach [a], T. Wattez [b], S. Van der Laan [a], H.J.H. Brouwers [a]

[a] Department of the Built Environment, Eindhoven University of Technology, P.O. Box 513, Eindhoven 5600 MB, the Netherlands
[b] Ecocem Materials Ltd, 4 Place Louis Armand, Paris 75012, France

ARTICLE INFO

Keywords:
BOF slag
Fine fillers
Potassium citrate
Hydration kinetic
Phase assemblage
PARC
Amorphous

ABSTRACT

This study investigates the hydration of basic oxygen furnace (BOF) slag pastes activated with tri-potassium citrate and the role of fine limestone and quartz fillers. Quantitative XRD, SEM–EDX with PARC, and mass balance modelling were combined to follow phase reactivity and hydrate formation. Brownmillerite (C_2F) and C_2S were identified as the main reactive phases. At 7 days, both contributed equally to hydrogarnet and C-S-H formation, while by 56 days C_2S became dominant. Fillers modified this balance: limestone mainly increased the overall hydrate content without altering the assemblage, whereas quartz enhanced late C_2S reactivity, raising C-S-H and hibschite proportions and lowering katoite. Hydrogarnets remained the major hydration product throughout, with a shift from katoite to silica-rich compositions over time. Deviations between modelled and experimental volatile contents highlight the influence of carbonation and variable hydrate stoichiometry, which are not captured in the current model.

1. Introduction

Cement production is a huge factor in anthropogenic climate change. It is responsible for approximately 8% of global CO_2 emissions. Reducing the environmental footprint of cement-based construction materials is a major challenge, and one widely investigated approach is the partial replacement of clinker with industrial by-products [1]. Among them, Basic Oxygen Furnace slag (BOF slag), when properly activated, offers significant potential due to its high availability, low cost, and latent hydraulic properties [2–6].

BOF slag is produced during the steel refining process and is mainly composed of the following oxides: CaO (30–50%), FeO/Fe_2O_3 (20–40%), SiO_2 (10–20%), MgO (4–10%), Al_2O_3 (1–7%), P_2O_5 (1–3%), MnO (0–4%), and TiO_2 (0–2%) [7–11]. Its solidified mineralogical composition is dominated by dicalcium silicate (C_2S), brownmillerite (C_4A,F), with low aluminium content, making it closer to C_2F in chemical composition, and wuestite containing iron magnesium, and manganese ((Fe,Mg,Mn)O). As minor phases, some magnetite (Fe_3O_4) is usually present, as well as lime in variable proportions (1–10 wt%) [7,9,10,12,13]. Unlike granulated blast furnace slag (GGBFS), which is largely amorphous and exhibits strong latent hydraulic and partial pozzolanic reactivity, BOF slag solidifies as a fully crystalline material and therefore shows no pozzolanic reactivity and only limited hydraulic reactivity. Consequently, it performs poorly as a Supplementary Cementitious Material (SCM). The absence of glassy phase and the predominance of crystalline C_2S - which is much less reactive than the C_3S phase present in Portland cement - further restrict its hydration potential. In addition, the presence of heavy metals (Cr, V) raises environmental concerns, as their leaching may occur during disposal or use in construction materials [2–4,14].

Nevertheless, when properly activated BOF slag can be used as a sole binder. Several strategies have been proposed in that respect. Mechanical activation through fine grinding increases the surface area and helps to form some amorphized C_2S that may react faster [15]. Chemical activation using complexing agents such as phosphates, oxalates, and citrates has also been shown to significantly enhance hydration [7,9,11,16]. One of the most promising chemical activators is tri-potassium citrate, which significantly improves the reactivity of BOF slag by promoting the dissolution of brownmillerite and wuestite. Citrate molecules may interact with the surface of the BOF slag grains, and control ions in pore solution by complexation and precipitation. Its use has been shown to significantly enhance early reactivity and improve compressive strength [7,8]. Additionally, it addresses the problems of false setting and reduces water demand through surface interactions, similar to the

* Corresponding author.
E-mail address: s.r.yvars@tue.nl (S. Yvars).

https://doi.org/10.1016/j.conbuildmat.2026.146271
Received 2 November 2025; Received in revised form 13 March 2026; Accepted 5 April 2026
Available online 9 April 2026

effect of a superplasticizer. The hydration products formed in a tri-potassium citrate binder are iron-containing hydrogarnets with a variable Si content ($C_3(A,F)S_xH_{6-2x}$), LDH-like phase identified as pyroaurite ($M_6(A,F)cH_{12}$), and C-S-H gel with a variable Ca/Si ratio [10]. It was demonstrated that such hydration products may incorporate and immobilize the heavy metals, considerably reducing their environmental impact [7,8]. Overall, the formation of hydration products that provide strength at an early age and the low water demand make BOF slag activated with tri-potassium citrate a performant binder.

Nevertheless, a previous study investigated the use of filler for improving C_2S reactivity and the overall performance of the citrate activated BOF slag binder, emphasizing the very slow reaction of C_2S in the system. It was demonstrated that the incorporation of fine fillers, such as ground quartz or limestone, in addition to 1 wt% of citrate, increases the compressive strength of the binder from 25% to 55%, between 7 and 56 days of hydration [17]. In OPC, fine fillers can act as nucleation sites for hydration products, especially for C-S-H gel, and enhance the kinetics of hydration [18–22]. However, in that work several key points in the use of fillers in BOF slag binder remain unclear. The impact of the filler on the reactivity of the C_2S and the associated effect(s) on the hydration product type and amounts is still not fully understood, especially compared to the effect on C_3S [23]. Furthermore, the resulting strength improvement is not fully explained due to methodological limitations and gaps in the current understanding of BOF slag hydration reactions. One of the main limitations stems from the difficulty of determining the exact composition of the X-ray amorphous matter found in BOF slag after milling with common techniques such as XRD and TG. Therefore, the differentiation between X-ray amorphous primary minerals and amorphous hydration products is not clearly establish and the role of fillers on C_2S reactivity and C-S-H formation is not explained.

To address these gaps, this study applies a model previously defined by Santos et al. [10], allowing for the assessment of the chemical composition of the amorphous matter in BOF slag cured pastes and the modelling of the hydration reactions that occur. This approach enables the role of fillers on C_2S reactivity to be investigated properly. This method combines advanced characterization techniques including quantitative X-ray diffraction (XRD), X-ray fluorescence (XRF), thermogravimetric analysis (TGA), and scanning electron microscopy coupled with energy-dispersive X-ray spectroscopy (SEM-EDX) and PhAse area Recognition Characterization (PARC). The study is performed on BOF slag pastes activated with tri-potassium citrate, used both as a necessary activator for brownmillerite and for ensuring practical applicability of BOF slag, and including limestone and quartz filler, with two different sizes and various dosages (3, 6, 9 vol%), all showing a beneficial effect on the binder performance, while the effect on BOF slag hydration remains poorly defined.

2. Materials and methods

2.1. Material

A BOF slag provided by TATA Steel, IJmuiden (The Netherlands), is used in this investigation. The material was received after being crushed to a 2–4 mm size and was therefore finely milled with a Retsch RS 300 XL disc mill at a constant speed of 912 min−1, for 20 min, to increase its specific surface area and enhance its reactivity.

Limestone and quartz fillers were used in two different sizes, named coarse and fine. The two limestone fillers were used as received, and the two quartz fillers were obtained by milling sand in a disc mill for 15 and 30 min, respectively.

The particle size distribution and the specific surface area of the raw materials were measured (*described in 2.3.*), and their size characteristics (d_{10}, d_{50}, d_{90}) are given in Table 1.

The chemical and mineralogical composition of the raw materials was assessed by performing X-Ray Fluorescence and quantitative X-Ray diffraction analysis (*described in 2.3*). These compositions are given for all the raw materials in Tables 2 and 3.

Table 1
Size and specific surface area of the raw materials.

Material	ID	SSA	d_{10} (μm)	d_{50} (μm)	d_{90} (μm)	< 1 μm (vol %)*
BOF slag	-	-	2.8	12.3	60.1	
Fine limestone	FL	2.09	1.2	4.4	11.1	6.6
Coarse limestone	CL	0.66	2.1	10.0	43.6	3.7
Fine quartz	FQ	5.13	0.3	4.3	21.5	26.6
Coarse quartz	CQ	3.21	1.7	10.5	40.1	6.6

* the volume percentage of filler particles with a size < 1 μm were used to calculate the amount of filler that might have been hidden in the "hydration products" phase detected with PARC, because of the resolution limit of the SEM EDX spectral imaging (1 μm pixel size).

2.2. Mix design

BOF slag paste samples were prepared containing 1 wt% of tri-potassium citrate and different dosages of filler (0, 3, 6, and 9 vol%). The fillers are replacing a part of BOF slag by volume in the mixtures (density calcite = 2.55 g/cm^3; quartz = 2.54 g/cm^3; BOF slag = 3.85 g/cm^3), and the corresponding mass substitution levels are 0, 2.01, 4.06, and 6.15 wt%. Table 4 summarizes the different mixture compositions.

The pastes were prepared in plastic jars and mixed for 2 min on a vibratory table. The jars were subsequently sealed to prevent any water evaporation or carbonation and kept at ambient temperature. At the chosen age (7 or 56 days) the samples were crushed and sieved in two different fractions: (1) the 2–4 mm pieces were stored to perform scanning electron microscopy (SEM), described in 2.3.) and the powder material passing 250 μm were used for thermogravimetric analysis and XRD. The hydration reaction of all the samples was stopped using the double solvent exchange method [24]. All of them were then properly stored in sealed jars before each analysis. The two curing ages were selected in this study in order to capture the main stages of BOF slag hydration previously reported in citrate-activated systems [11,17]. Earlier studies indicate that brownmillerite reacts mainly during the first days of hydration, while the slower hydration of C_2S becomes more significant at later ages, making these two curing times representatives of the early and later stages of the reaction investigated in this study. Intermediate ages could provide additional insight into the progression of these reactions and would be valuable for future investigations.

Table 2
Oxide composition of the raw materials as determined with XRF.

Oxide (wt%)	BOF slag	Limestone	Quartz
CaO	41.30	69.10	-
FeO/Fe_2O_3*	31.00	0.06	3.35
SiO_2	10.88	0.31	94.13
MgO	5.32	-	-
MnO	5.28	0.08	0.03
Al_2O_3	1.50	0.15	2.08
TiO_2	1.42	-	-
V_2O_5	1.07	-	-
P_2O_5	1.01	-	-
Cr_2O_3	0.31	-	0.42
SrO	-	0.01	-
LOI/GOI**	-0.90	30.30	0

* The proportion of Fe_2O_3 of Fe_{total} in the slag is approximately 0.25 [12]; however, due to the heating to 1000 °C during sample preparation to remove the volatiles, all FeO is present as Fe_2O_3 in the analysed samples.

** LOI and GOI refer to Loss and Gain on ignition and correspond to the weight of volatile compounds. It is common to record a GOI for BOF slag due to the oxidation of FeO to Fe_2O_3.

Table 3
Mineralogical composition of the raw materials.

Phase (wt%)	Formula	BOF slag	Quartz	Limestone
Brownmillerite	$Ca_2(Al, Fe)_2O_5$	16.7	-	-
C_2S	Ca_2SiO_4	40.0	-	-
Wuestite	(Mg,(Fe)O	18.4	-	-
Magnetite	Fe_3O_4	6.3	-	-
Lime	CaO	0.4	-	-
Calcite	$CaCO_3$	0.7	-	84.9
Quartz	SiO_2	-	71.3	2.5
Iron	Fe	-	1.3	
Amorphous	-	18.6	27.5	12.6

Table 4
Compound proportions of the mixtures.

Sample ID	BOF slag content (wt%)	Filler amount (wt%)	Tri-potassium citrate dosage (wt%)*	Water to binder ratio	Water to BOF slag ratio
Ref	100	0	1	0.18	0.180
FL,CL, FQ, CQ3**	97.99	2.01	1	0.18	0.184
FL,CL, FQ, CQ6**	95.94	4.06	1	0.18	0.188
FL,CL, FQ, CQ9**	93.75	6.15	1	0.18	0.192

* the amount of tri-potassium citrate is kept constants for all the samples and corresponds to 1 wt% of the total mass of powder, not only the mass of BOF slag.
** FL, CL, FQ and, CQ for Fine limestone, Coarse limestone, Fine quartz and Coarse quartz, respectively.

2.3. Methodology

2.3.1. Particle size distribution

The particle size distribution (PSD) of the raw materials was measured using laser diffraction with a Malvern Mastersizer 2000 in a liquid medium. Isopropanol was used to avoid possible reactions of BOF slag during the measurement, and ultrasound was applied to disperse particle agglomerates. The resulting volume distributions were used to compare the particle sizes of the materials and confirm the similarity between the fine fillers (FL and FQ) and the coarse fillers (CL and CQ).

2.3.2. Oxide composition

The bulk oxide composition of the raw materials was determined by X-ray fluorescence (XRF). Prior to analysis, powder samples were heated to 1000 °C for 10 h to determine the loss or gain on ignition (LOI/GOI) and remove volatile components. The powders were then fused into beads and analysed using a PANalytical Epsilon 3 spectrometer with the OMNIAN standardless method.

2.3.3. Mineralogical composition - Quantitative X-Ray diffraction (Q-XRD)

The crystalline phase composition was determined by quantitative X-ray diffraction. Powder samples were intermilled with 10 wt% silicon metal powder (XRD-Mill McCrone, RETSCH), used as an internal standard to quantify the amorphous fraction. The powders were backloaded into sample holders to minimise preferred orientation. XRD measurements were performed using a Bruker D4 ENDEAVOR diffractometer with Co radiation ($\lambda = 1.79$ Å). Data were collected over a 2θ range of 12–80° with a step size of 0.014° and a counting time of 1 s per step. Phase quantification was carried out using the Rietveld method implemented in TOPAS Academic v5.0. The structural data used for the analysis are listed in Tables 5–7.

2.3.4. Thermogravimetry (TGA)

Thermogravimetric analysis was used to evaluate differences in the hydrate assemblage between the samples. Approximately 100 mg of powder was analysed using a Netzsch Jupiter STA 449 F1 thermogravimetric analyser. Measurements were conducted under a nitrogen atmosphere by heating the samples from 40 to 1000 °C at a rate of 20 °C/min.

Table 5
XRD phase structural data.

Phase	Formula	ICSD	PDF
Brownmillerite	$Ca_2(Al,Fe)_2O_5$	-	04–014–6627
α'-C_2S	Ca_2SiO_4	81097	
Larnite	Ca_2SiO_4	81096	
Fe/Mg Wuestite	Fe(Mg)O/Mg(Fe)O	67200	
Magnetite	Fe_3O_4	30860	
Lime	CaO	28905	
Portlandite	$Ca(OH)_2$		01–076–0571
Hydrogarnets	$Ca_3(Al, Fe)_2(OH)_{12}$	66274	
Pyroaurite	$Mg_6Al_2CO_3(OH)_{16}.4H_2O$		01–074–1513
Calcite	$CaCO_3$	80869	
Quartz	SiO_2		01–070–3755

Table 6
Volume percentage of filler particles included in the hydration product phase.

Sample ID	3	6	9
FL	1.65	3.35	5.02
CL	0.87	1.75	2.62
FQ	1.60	3.20	4.80
CQ	0.89	1.79	2.70

2.3.5. Scanning electron microscopy with energy dispersive X-Ray Spectroscopy (SEM- EDX)

Microstructural observations and elemental analyses were carried out using a JEOL JSM-7001F field-emission scanning electron microscope equipped with two 170 mm^2 Oxford SDD detectors. Samples were prepared by embedding fragments of hardened paste in epoxy resin (Struers EpoFix), polishing the mounts without water to avoid phase alteration, and coating the surfaces with a 10 nm carbon layer. Elemental maps were obtained by EDX spectral imaging at an accelerating voltage of 15 kV and a beam current of 10 nA. The spatial resolution was 1 μm per pixel, with 1 image fields of 512 × 382 pixels per sample and an acquisition time of approximately 30 min per field.

2.3.6. Phase Area Recognition Characterization (PARC)

PARC software was used to identify and quantify phases from the SEM-EDX spectral images [10,25-27]. The software groups pixels with similar elemental signatures into compositional clusters, allowing identification of mineral phases and estimation of their area fractions. Using this method, the remaining primary BOF slag phases were identified as C_2S, brownmillerite, and a wuestite-magnetite group. Calcium-rich phases such as free lime, portlandite, carbonates and possible citrate compounds form another compositional group. Filler particles larger than the spatial resolution (1 μm) were also identified. Hydration products form a composite PARC group located between the unreacted slag grains and filler particles. This group contains C-S-H gel, hydrogarnets [28] and pyroaurite [29], which cannot be separated individually because of their small size and similar elemental compositions.

2.3.7. Mass balance calculation

To determine the phase assemblage and the composition of the hydration products, the analytical results from PARC, XRD, TGA and XRF were combined using a mass-balance model following the approach proposed by Santos et al. [10]. The area fractions obtained from PARC were converted to mass fractions using the densities of the phases

Table 7
Legend of the phase maps.

Colour code	PARC group
	Hydration products
	Brownmillerite
	C_2S
	Wuestite + Magnetite
	Free lime
	Limestone + Portlandite + Carbonates
	Quartz

determined from XRD. Average chemical compositions measured by EDX spectral imaging were then used to perform a series of least-squares calculations in order to:

1. Estimate the initial phase composition of the raw BOF slag
2. Quantify the consumption of the primary slag phases
3. Determine the distribution of hydration products within the composite hydration product phase

For the calculation, elements assumed to substitute for one another in the model were grouped as follows:

- Si, P, V, Ti
- Al, FeIII, Cr
- Mg, FeII, Mn
- Ca, Na, K

These cations were distributed among four hydration products with fixed representative formulas: pyroaurite, Fe-katoite, hibschite, and C-S-H. The calculation determines the relative proportions of these phases that best reproduce the measured chemical composition of the hydration product domain.

2.3.8. Reaction based hydration modelling

The overall hydration behaviour was interpreted using a simplified reaction model describing the main processes occurring in the system. Four representative reactions were considered and are represented as follows:

(i) Hydrogarnet formation:

$$G\left[C_2F + 2C_2S + H_{(9.6-2.3x)} = C_3FS_xH_{(3-x)_2} + (1.7x - 0.4)CH + (2-x)C_{1.7}SH_2\right]\# \quad (1)$$

(ii) Pyroaurite formation:

$$J[C_2F + 6M + 14H + c = M_6FcH_{12} + 2CH]\# \quad (2)$$

(iii) Wuestite oxidation - Brownmillerite restoration:

$$K[2f + 2CH = C_2F + 2H]\# \quad (3)$$

(iv) C-S-H gel formation:

$$N[C_2S + 2.3H = C_{1.7}SH_2 + 0.3CH]\# \quad (4)$$

With: f=FeO and F=Fe_2O_3, M=MgO and MnO, S= all elements substituting for Si, (P, Ti, V and V), and F all cation interchangeable with Fe (Al and Cr).

The coefficients of these reactions (G, J, K and N) were determined by fitting the calculated phase assemblage obtained from the mass-balance model. Parameter x represents the silica content of hydrogarnets.

2.3.8.1. Estimated volatile content in the hydration products. To evaluate the consistency of the model, the predicted amounts of H_2O and CO_2 associated with the calculated hydration products were compared with the experimental mass losses measured by TGA. Because the samples contain tri-potassium citrate and limestone fillers, their thermal decomposition also contributes to mass loss and must be accounted for. The total mass loss in the chosen ranges is due to hydration product volatile losses [24,30–33], but also to the loss associated with the decomposition of the limestone filler [34,35] and tri-potassium citrate activator [36,37]. It should be noted that quartz is thermally stable. The simplified decomposition reactions used for these corrections are given in Eqs. 5 and 6.

Tri-potassium citrate decomposition:

$$2K_3C_6H_5O_{7(s)} \rightarrow 2K_2CO_{3(s)} + K_2O_{(s)} + 9C_{(s)} + \quad 5H_2O_{(g)} + \quad CO_{2(g)}(+ \textit{volatiles organics})\# \quad (5)$$

Limestone decomposition:

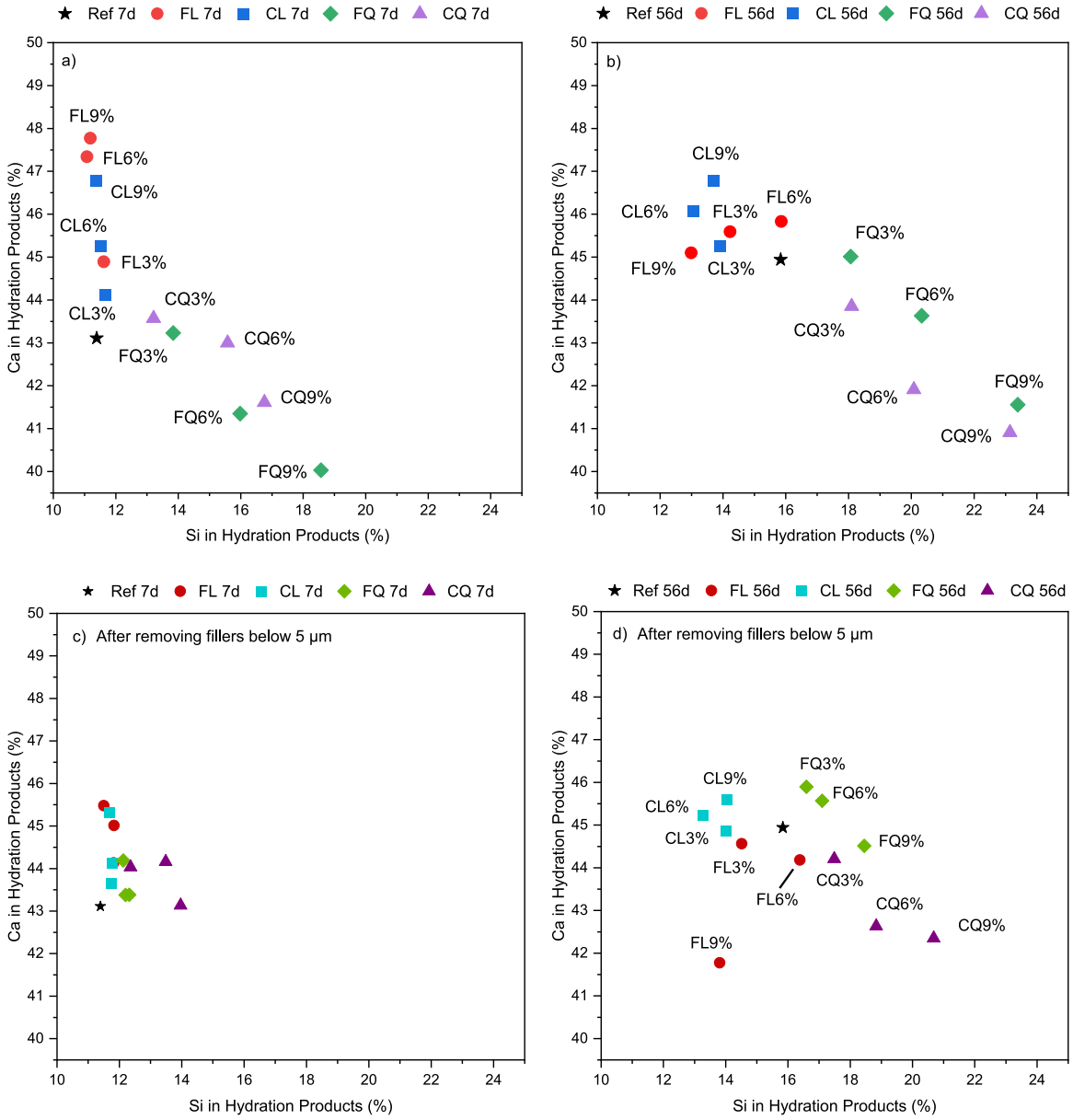

Fig. 1. Calcium versus Silica content (wt%) in the hydration product phase (detected with PARC) of BOF slag paste samples containing fillers, (a) and b) 7 days and 56 days before removing the filler with size < 5 µm, c) and d) after removing filler with a size < 5 µm.

$$CaCO_{3(s)} \rightarrow CaO_{(s)} + CO_{2(g)}\# \quad (6)$$

The theorical losses associated with citrate decomposition correspond to 14.7 wt% H_2O and 7.2 wt% CO_2. In the analysed samples this represents 0.147 wt% and 0.072 wt%, respectively. For limestone, the CO_2 loss was estimated using the measured LOI value of 30 wt%, corresponding to 0–1.9 wt% CO_2 depending on the filler dosage.

2.3.9. *Correction for submicron filler particles*

Because the spatial resolution of SEM-EDX spectral imaging is approximately 1 µm, filler particles smaller than this size cannot be distinguished from the hydration product phase in PARC analysis. As a result, a fraction of the filler may be incorporated into the measured composition of the hydration product group. Fig. 1**a), b)** show that the measured Ca and Si contents increase with limestone and quartz dosage, respectively. To account for this effect, a correction was applied based on the particle size distribution of the fillers. Although the analytical resolution of SEM imaging is approximately 1 µm, a threshold of 5 µm was selected for the correction. This larger threshold was chosen to minimise uncertainties associated with: (1) particle morphology when projected in two dimensions and (2) mixed pixels at the filler-hydrate interface, where hydration products precipitated on the surface of filler particles may be partially detected together with the filler signal.

The proportion of filler particles smaller than 5 µm was therefore estimated from the particle size distributions of the fillers. This fraction was assumed to be incorporated into the hydration product phase and was used to correct both the phase proportions and the chemical composition using Eqs. 7 and 8. The corrected values were then used in the mass-balance calculations and are reported in Appendix C Tables C1, C2. The calcium and silica contents in the corrected hydration product compositions are presented in Fig. 1**c), d)**, which show a decrease in the overall Ca and Si contents after correction and a reduced compositional range between samples, particularly at 7 days, indicating that part of the initial variability was associated with the presence of fine filler particles.

$$Oxide\,[HP]_{norm} = \frac{Oxide[HP]_{PARC} \times Area[HP]_{PARC} - Oxide[F]_{XRF} \times Area[F]_{calc}}{Area[HP]_{PARC} - Area[F]_{calc}} \# \quad (7)$$

With, "Norm" for normalized value, "PARC" for oxide of phase percentage obtained with PARC, "XRF" for oxide percentage from XRF analysis, "calc" for the adjusted area percentage based on filler size.

$$Oxide\,[Ca.p]_{norm} = \frac{Oxide[Ca.p]_{PARC} \times Area[Ca.g]_{PARC} + Oxide[F]_{XRF} \times Area[F]_{calc}}{Area[Ca.g]_{PARC} + Area[F]_{calc}} \# \quad (8)$$

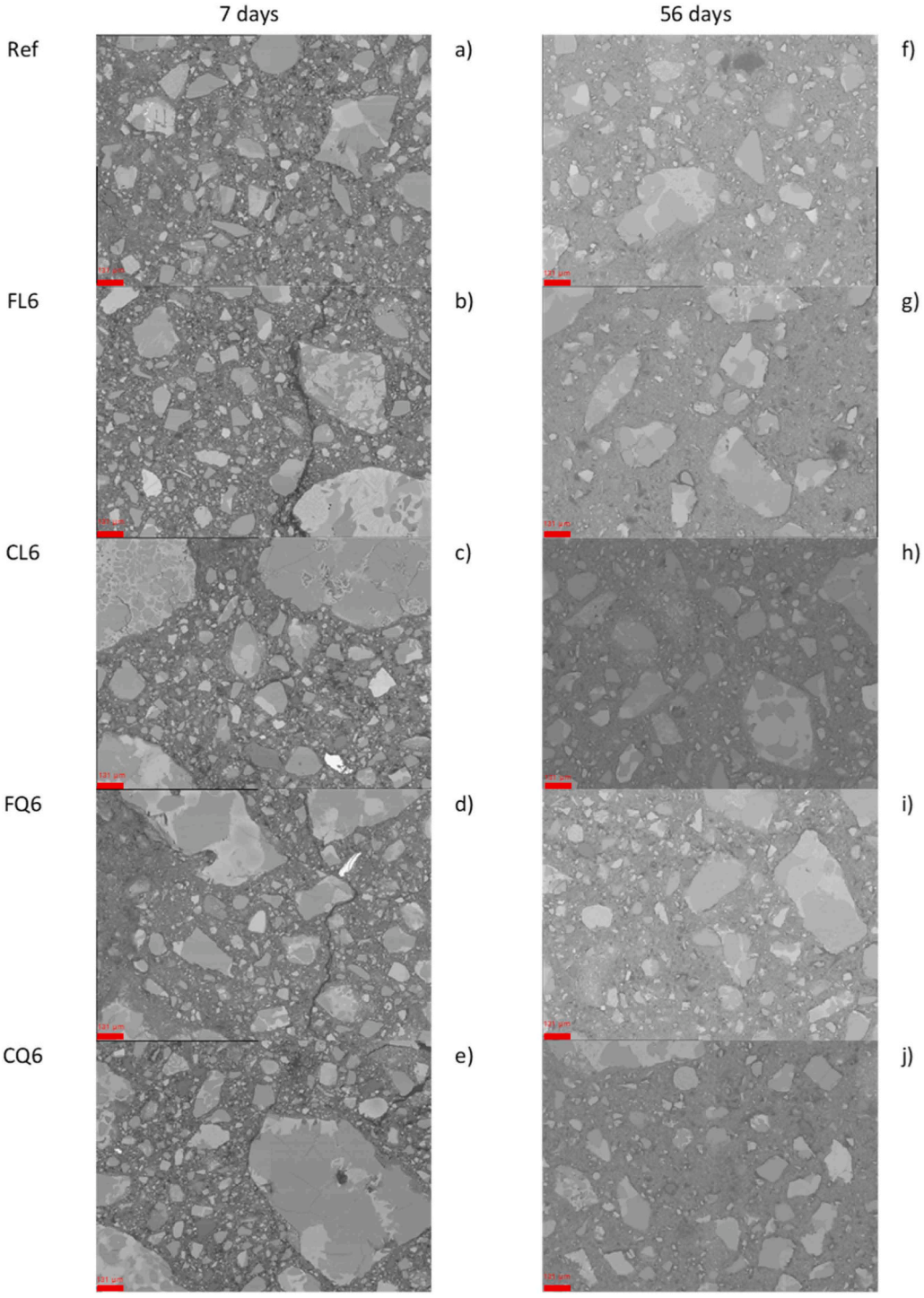

Fig. 2. SEM images of the samples containing 6% of filler at 7 and 56 days (a) and f) Reference; b) and g) fine limestone; c) and h) coarse limestone; d) and i) fine quartz; e) and j) coarse quartz). Scale bars account for 131 μm.

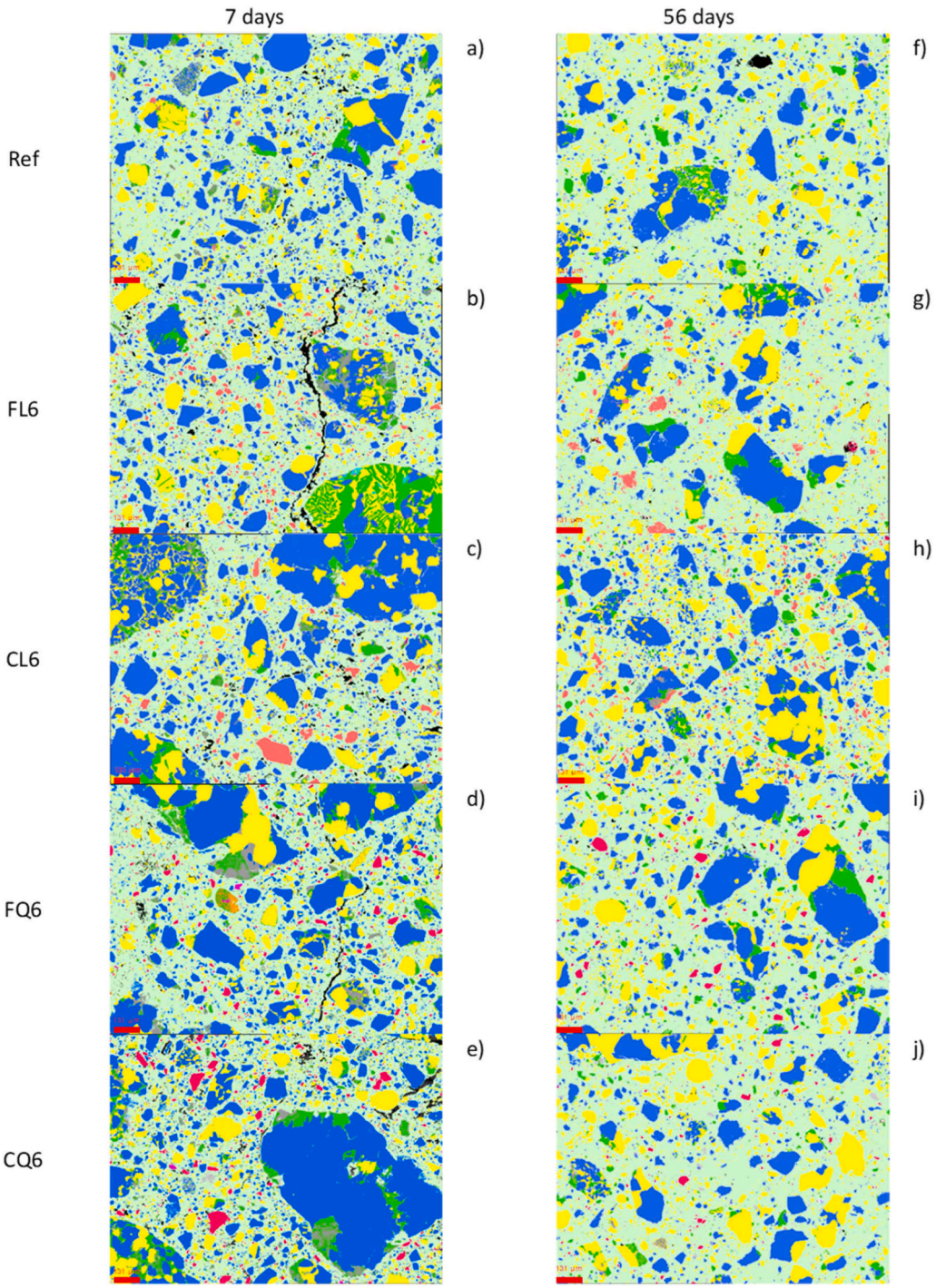

Fig. 3. Phase maps obtained with PARC software of the samples containing 6% of filler at 7 and 56 days (a) and f) Reference; b) and g) fine limestone; c) and h) coarse limestone; d) and i) fine quartz; e) and j) coarse quartz). Scale bars account for 131 μm.

"HP" for hydration products, "F" for filler, "Ca-g" for Ca-rich parc group.

2.3.10. Model assumptions and limitations

The modelling approach used in this study relies on several simplifying assumptions that may influence the calculated phase proportions. Because the hydration products are represented by fixed stoichiometric compositions, variations in the real composition of hydrogarnets or C-S-H may be expressed in the model as changes in the relative proportions of these phases. Consequently, compositional variability of hydrogarnets and C-S-H may be expressed in the model as changes in their calculated phase proportions.

Uncertainty may also arise from the correction applied for fine filler particles. If a small fraction of filler remains incorporated in the hydration product domain, the measured chemical composition used as input for the mass-balance calculation may be slightly enriched in the corresponding elements (Si in quartz-containing systems or Ca in limestone-containing systems). This could influence the calculated distribution of elements between the modelled hydration products.

In addition, carbonation reactions are not explicitly considered in the model. If very fine carbonate precipitates are present, they may be incorporated into the hydration product domain detected by PARC and locally increase its Ca content. This may slightly influence the calculated

distribution of Ca between the modelled hydration products.

These aspects may therefore affect the absolute values of the calculated phase proportions. For this reason, the modelling results are interpreted primarily in terms of relative trends, comparisons between systems and reaction evolution, rather than as exact quantitative amounts of individual hydration products.

3. Results and discussion

3.1. Microstructure and phase maps

Fig. 2 and Fig. 3 present the SEM images and the phase maps obtained from the SEM micrographs using PARC software, in which different colours are assigned to distinguishable "mineral phases", respectively. Due to similarities between the samples, only the images obtained for the reference and the samples containing 6% of filler are presented in the following section. The data of the 3 and 9% filler-containing samples are available in the Appendix, Figs. A1–2 and A3–4, respectively

Fig. 2 reveals a similar microstructure across all the samples. The lighter and more homogeneous matrix in the images may reflect a denser hydration product phase. However, care should be taken because the applied contrast and brightness settings for the BSE image were not kept the same for all BSE images.

The phase maps present in Fig. 3 show that BOF slag grains contain C_2S, brownmillerite and wuestite/magnetite were identified. Quartz and limestone grains are observed in the corresponding quartz and limestone-containing samples, respectively. The intergranular regions are occupied by hydration products, which are represented as a single PARC group in the maps. It should be noted that the phase maps have certain limitations: (1) wuestite and magnetite cannot be differentiated due to their similar elemental composition; (2) limestone, portlandite, calcium carbonates and free lime exhibit similar chemical composition, making it impossible to distinguish them individually with this method; (3) The "hydration product" contains all crystalline and/ or amorphous hydration products, such as hydrogarnets, pyroaurite, and C-S-H gel, as well as submicron sized filler. These hydration products cannot be separated due to their comparable elemental composition, mainly Fe, Si and Ca, and their size below the EDS resolution of around 1micron. Large area phase mapping using PARC methodology provided both area percentages and a very accurate chemical composition of each phase, based on EDX Spectral Image measurements. Because the analysed areas are limited the area% of each phase are not representative for the overall phase amount. As a result, they are not used in the calculations and are only presented in Appendix, Table A1.

3.2. Primary slag phase chemical composition

The chemical composition of the main primary phases identified by PARC (brownmillerite, C_2S, and the wuestite/magnetite group) was evaluated using EDX spectral imaging. The chemical formulas of the phases were calculated by normalizing the cation contents, allowing comparison with their ideal compositions and assessment of possible substitutions. Detailed compositions for all samples are reported in Appendix A Tables A2-A4. To investigate compositional trends between samples and hydration ages, the elemental compositions were also analysed using a centred log-ratio (CLR) transformation, which allows meaningful comparison of compositional data constrained to a constant sum. The CLR-transformed values for the main elements are presented in Fig. 4 for the reference and mixtures containing fine fillers, while the corresponding numerical values are given in Appendix A Tables A5-A10. The results obtained for mixtures containing coarse fillers are presented in Appendix A Figure A5 and show similar overall trends.

3.2.1. Brownmillerite chemical composition

Brownmillerite in BOF slag differs from the conventional C_4AF

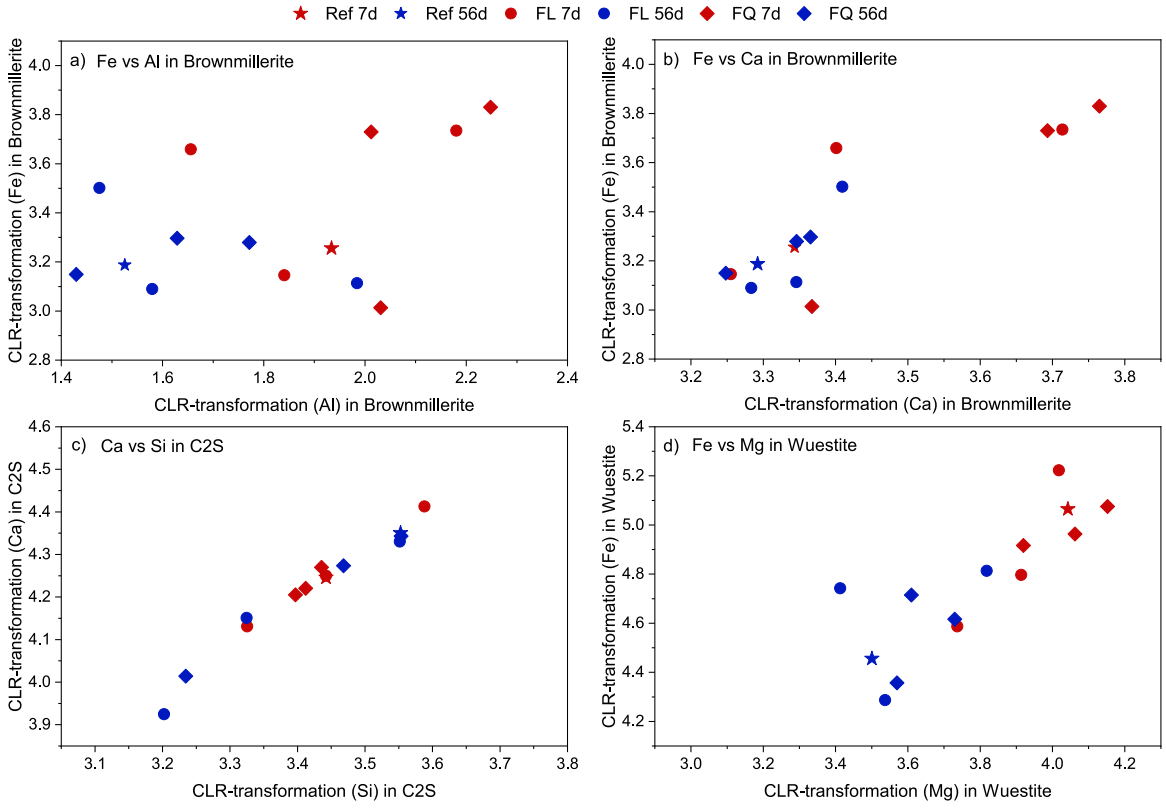

Fig. 4. Centred Log Ratio (CLR) of the average chemical composition of the primary phases remaining in the reference and the samples containing fine fillers at 7 days and at 56 days, (a) Fe vs Al in brownmillerite; b) Fe vs Ca in brownmillerite; c) Ca vs Si in C_2S; d)FeO vs MgO in wuestite/magnetite.

composition due to its high iron content. Based on PARC analysis, its composition can be approximated as $Ca_4(Fe, Al, Ti, V)_4O_{10}$, with Ca and FeIII as the dominant elements

The CLR-transformed data in Fig. 4**a-b** show that the most significant change is observed for Fe, which decreases between 7 and 56 days, indicating preferential dissolution of Fe from brownmillerite during hydration. This behaviour is consistent with the known interaction of citrate promoting iron-bearing phases dissolution.

The variation of the CLR-transformed elemental compositions with filler dosage is illustrated in Fig. 5, and the linear regression data are reported in Appendix A Tables A11–1. These results show that, at 7 days, limestone-containing systems tend to retain more Fe in the residual brownmillerite, whereas quartz-containing systems show slightly greater Fe depletion. These differences become less pronounced at 56 days, suggesting that filler effects mainly influence the early hydration stage. One possible explanation relates to the dosage of the activator. In the present study, the amount of tri-potassium citrate is kept constant relative to the total powder mass. Because fillers replace part of the BOF slag, the effective citrate-to-slag ratio increases in mixtures containing fillers (0.180, 0.184, 0.188, 0.192 when adding 0, 3, 6, and 9 vol% of filler). Consequently, a higher amount of activator is available per unit mass of reactive slag, which may enhance the dissolution of Fe-bearing phases during the early stages of hydration.

3.2.2. C_2S chemical composition

The C_2S, exhibits a relatively stable composition across all samples and ages. The calculated Ca/Si ratios remain within the range 1.87–1.92, indicating only minor compositional variation during hydration. Silicon is consistently slightly below the ideal value due to partial substitution by elements such as P, V, Ti, Al and Fe, which is typical for slag-derived C_2S.

The CLR-transformed data (Fig. 4**c**) show a strong correlation between Ca and Si contents, indicating that dissolution of C_2S occurs approximately stoichiometrically, without significant change in the internal Ca/Si balance of the residual phase. Similar relationships are observed for mixtures containing coarse fillers (Appendix Figure A2). Unlike brownmillerite, no clear influence of filler type or dosage on the chemical composition of the remaining C_2S is observed. The compositional trends are therefore mainly attributed to gradual dissolution of the phase rather than to changes in reaction conditions.

3.2.3. Wuestite/ Magnetite group chemical composition

The wuestite/magnetite group corresponds to a mixed Fe–Mg oxide phase that can be approximated as a solid solution of (Fe,Mg,Mn)O with minor Fe_3O_4. The dominant cations are Fe^{2+}, Mg^{2+} and Mn^{2+}, with smaller contributions from Fe^{3+} associated with the magnetite component.

The CLR values for Fe and Mg (Fig. 4**d**) show a wider distribution than for the other phases. A general decrease in Fe content between 7 and 56 days indicates partial dissolution of Fe from the phase, while Mg remains comparatively stable. This behaviour suggests a preferential redistribution of Fe relative to Mg, which may reflect the higher mobility of Fe in citrate-activated systems. Comparable trends are observed in the mixtures containing coarse fillers (Appendix Figure A2).

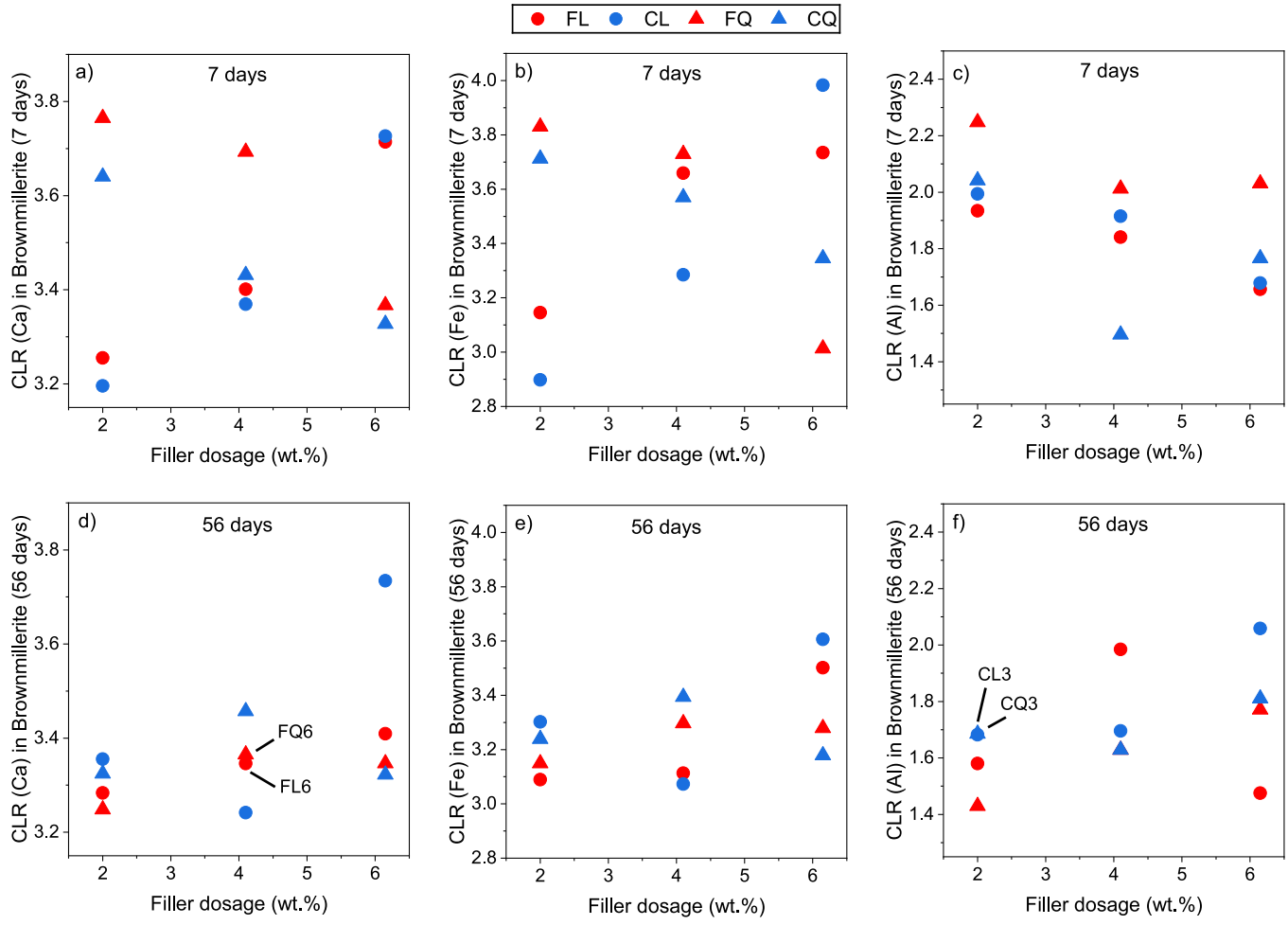

Fig. 5. Linear regressions between the CLR value of the major elements in brownmillerite depending on the filler dosage (a),d) CLR(ca) at 7 and 56 days; b), e) CLR (Fe) at 7 and 56 days, c), f) CLR(AL at 7 and 56 days).

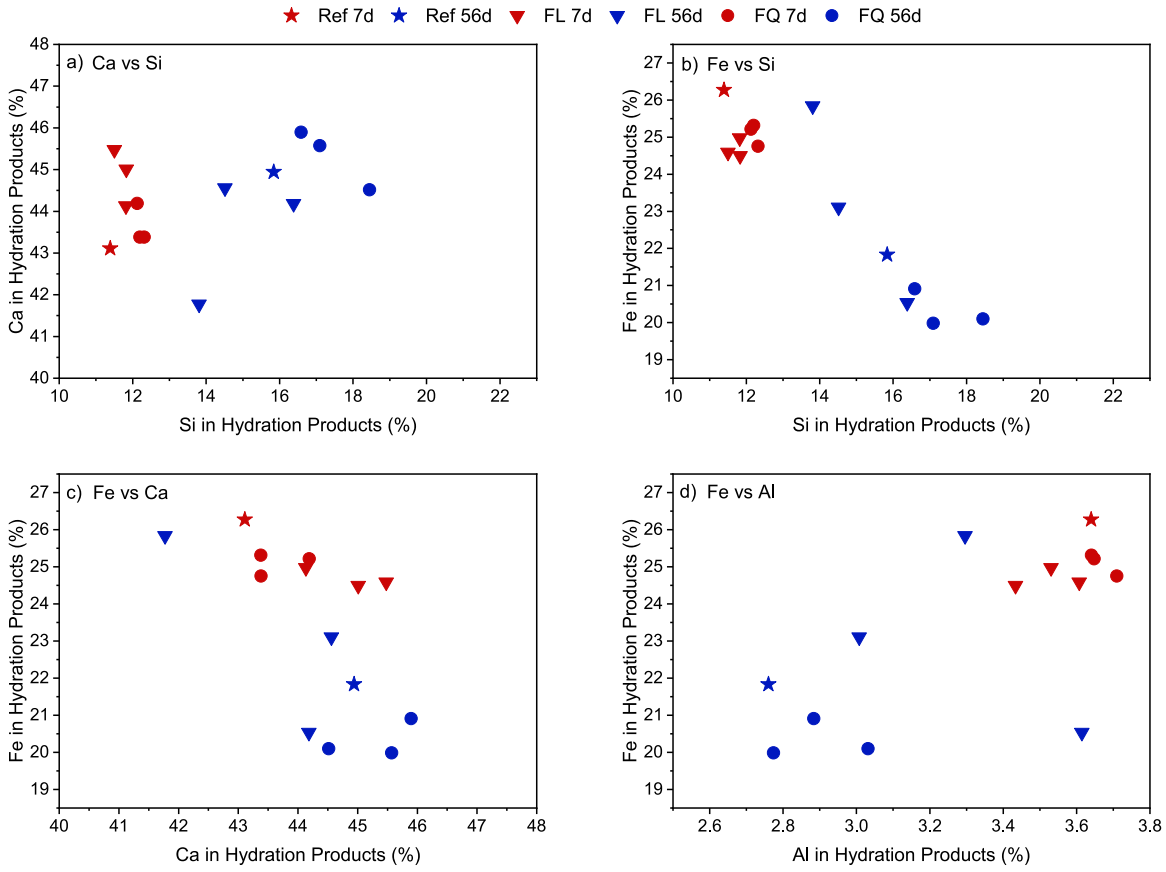

Fig. 6. Tracking of the major element detected in the hydration product phase of the reference and the samples containing fine fillers (a) Ca vs Si; b) Fe vs Si; c) Fe vs Ca; d) Fe vs Al).

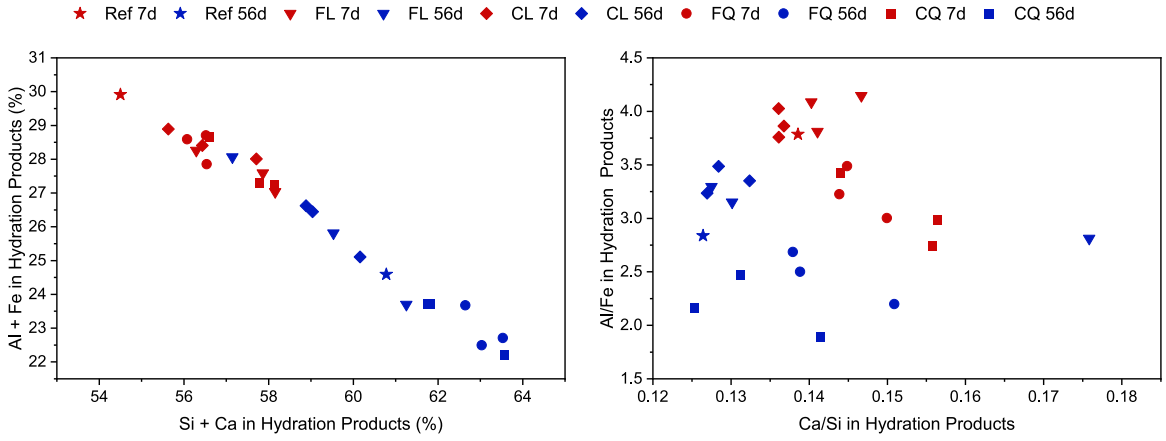

Fig. 7. Comparison between the elements provided mainly by Brownmillerite reaction Al + Fe) and C2S reaction (Si + Ca) in the different samples at 7 and 56 days.

3.3. Evolution of the hydration product chemical composition

Fig. 6 presents the chemical composition of the hydration products formed in the reference and the samples containing fine fillers at 7 and 56 days. Similar trends were observed for coarse fillers, and the data plots are presented in Appendix A Figure A6. The Ca content remains stable over time ranging from 41.5% to 46%. A shift is observed in the Fe content. While the range at 7 days is very narrow (23.5–26%), it spreads and slightly decreases at 56 days (19.5–26%). The Al content also changes with time, showing similar values in all the samples at 7 days (3.4–3.8%) that become slightly lower at 56 days and slightly more variable (2.6–3.6%). In contrast, a significant increase is observed in the Si content between 7 and 56 days, which rise from a range of 11–14% to 14–21%, respectively. As observed with the other elements the Si amount is very stable across the samples at 7 days while greater variations are detected at 56 days. Overall, these results suggest that the hydration product phase is enriched with Si at later age. This is accompanied by the slight decrease in the relative amounts of Fe and Al (closure effect) that also reveal that the content of those two elements is no longer increasing. In comparison, the Ca content staying stable with time indicates that Ca is still incorporated in the hydration products, but less than Si, making the relative amount stable. This is also observed in

Table 8
Phase composition of BOF slag raw material, estimated with different methods, XRD quantification and mass balance calculation from PARC chemical compositions.

Content (wt%)	Average* starting composition from PARC	Standard deviation**	XRD	XRD with distributed amorphous content***
Wuestite + Magnetite	33.1	2.1	24.7	33.3
Brownmillerite	19.5	4.7	16.7	19.6
C2S	46.0	2.5	40	46.2
Free lime	1.3	1.4	0.4	1.3
Amorphous	-	-	18.6	-

* the average starting composition is calculated from the results obtained with all the samples that was very similar, the individual results are presented in the Appendix in Table A13.

** the standard deviation values are representing the deviation between the starting composition estimated with all the sample and the average reported.

*** PARC average starting composition was used to estimate what proportion of the amorphous matter are possibly coming from each of the 4 phases, this proportions were used considering the amorphous content detected with XRD and distributed among the different phases to estimate the phase content of the raw BOF slag, including the possible X-Ray amorphized phase [10,17].

the Fig. 7 showing the evolution of Fe + Al versus Ca + Si in the hydrate phase at 7 and 56 days. At 7 days the hydration products are iron rich while they become silica richer after 56 days. This is in accordance with the knowledge about BOF slag hydration in citrate activated systems. The brownmillerite reacts mostly within the 7 first days, at later ages, the main reactive phase is C_2S that is known to react slower, adding more Ca but especially Si to the hydrate composition. The greater increase in Si compared to Ca might be due to a promoted mobility of Ca compared to Si in the presence of citrate [9]. Moreover, it should be noted that the filler nature, size or dosage does not seem to influence the elemental composition of the hydration products at 7 days, but may have an influence at later ages, mainly by promoting C_2S reactivity.

3.4. Mass balance calculation

3.4.1. Starting phase composition

For all the samples individually, the PARC data were used to first recalculate the starting phase amounts of the raw BOF slag, as described in Section 2.3.7.1. The phase proportions obtained for each sample were very similar as the same BOF slag was used for all samples and are reported in Appendix in Table A13. The results are therefore attesting the accuracy of the chemical composition of the phases and the calculation methods.

Table 8 presents the average phase proportions, the corresponding standard deviation values and the XRD quantification of the raw BOF slag. It is shown that the phase contents calculated from PARC are always above the phase contents detected with XRD due to the amorphous content of 18.6 wt% detected via QXRD. PARC cannot detect amorphous phases as the identification is made purely based on chemical composition. The differences between the 2 compositions suggest that a part of the reactive crystalline phase were amorphized during the milling of the material, in accordance with [11,15,17].

3.4.2. Phase contribution in the reaction

Fig. 8 presents the normalized contribution of the primary slag phases to the formation of hydration products at 7 and 56 days. The contribution of the wuestite/magnetite group remains low in all samples, ranging from approximately 6–22%. This behaviour reflects the limited reactivity of wuestite even in the presence of citrate and the essentially inert nature of magnetite.

In contrast, brownmillerite and C_2S dominate the hydration reactions. At 7 days both phases contribute similarly to hydration product formation (about 40–45% each). At 56 days a clear shift occurs: the contribution of brownmillerite decreases to 17–35% while the contribution of C_2S increases to approximately 50–60%. This evolution is consistent with the known hydration behaviour of BOF slag systems, where brownmillerite reacts rapidly at early age to form hydrogarnets whereas C_2S reacts more slowly and becomes increasingly important at later stages. It should be noted that the calculated phase contributions are derived from the mass-balance model described in **Section 2.3** and therefore depend partly on the assumed stoichiometry of the hydration products. However, the consistent trends observed between samples and curing ages indicate that the relative evolution of the reactions is robust even if the exact phase proportions may vary. The presence and nature of fillers influence this phase evolution, particularly the reactivity of C_2S. In systems containing limestone, C_2S already appears as the main contributing phase at 7 days, indicating a moderate acceleration of its hydration. Limestone particles provide additional nucleation sites for hydrate precipitation and may also temporarily act as a calcium sink [23,38], favouring the continued dissolution of C_2S. In contrast, samples containing quartz filler exhibit the highest relative C_2S contribution at 56 days. This indicates a delayed, but enhanced C_2S reactivity compared with both the reference system and limestone-containing samples.

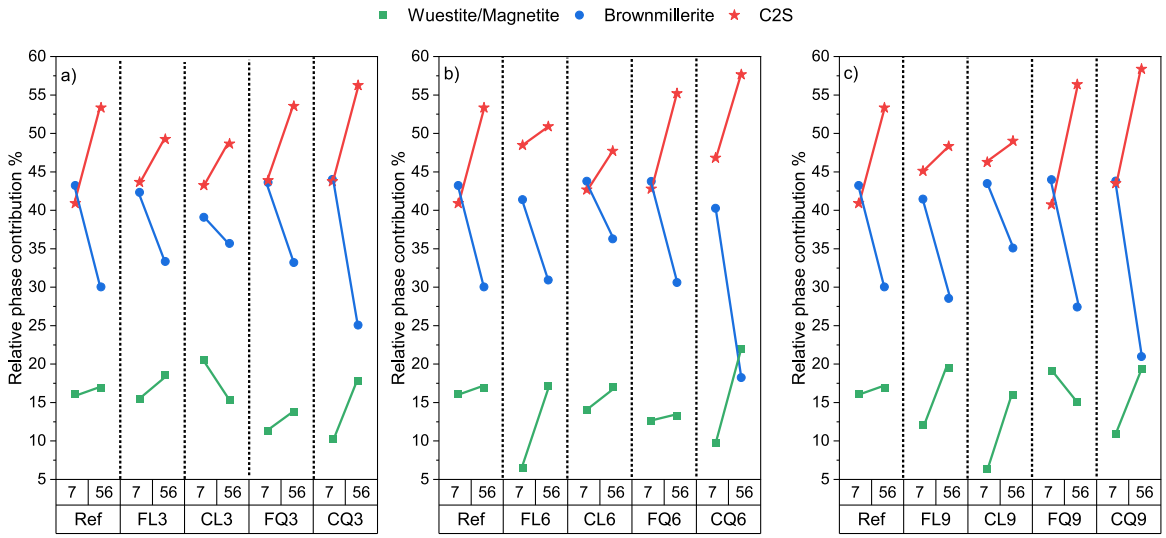

Fig. 8. Relative primary slag phase contribution to the hydration product in each sample at 7 and 56 days (a) 3% filler; b) 6% filler; c) 9% filler).

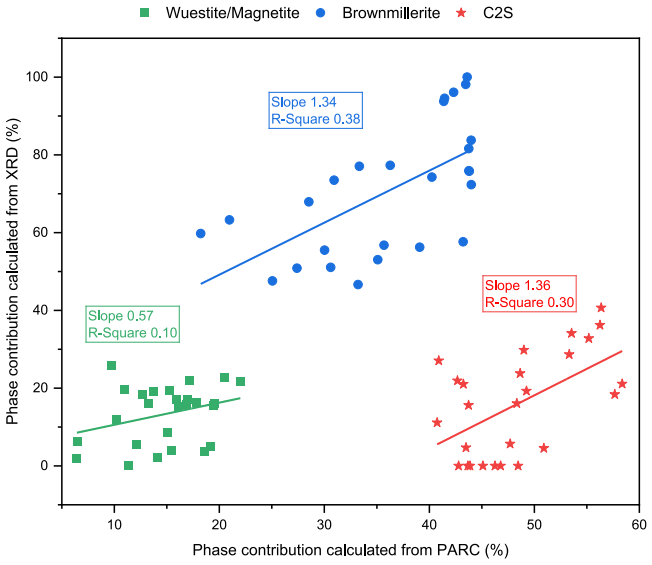

Fig. 9. Comparison of the phase contributions from PARC/ mass balance calculation and the phase contribution calculated from XRD data.

Quartz is generally considered chemically inert in cementitious systems and therefore likely acts mainly through a physical nucleation effect, providing additional surfaces for C-S-H precipitation and facilitating the continued dissolution of C_2S at later ages. However, a minor contribution from partial quartz dissolution, which could release silica-bearing species into the pore solution, cannot be completely excluded. If present, this additional silica could contribute to the formation of more silica-rich hydrates such as C-S-H or hibschite, however such a contribution is expected to be minor. The increase of the effective citrate/BOF slag ratio may contribute to the enhanced dissolution of some Fe-bearing phases, particularly at early ages. However, because brownmillerite reacts mainly within the first days of hydration and the relative change in citrate concentration remains small, this effect is not expected to significantly alter the overall hydration pathways observed in the present study.

The phase contributions obtained from the PARC-based mass balance were compared with phase consumption calculated from quantitative XRD (Fig. 9). Linear regression analysis shows similar trends for C_2S and brownmillerite (slopes of 1.34 and 1.36), although correlations remain moderate. For the wuestite/magnetite group the correlation is weaker.

These differences likely reflect the limitations of quantitative XRD in detecting small compositional changes and poorly crystalline phases [24], while PARC derives phase contributions from chemical composition data and is therefore more sensitive to partial dissolution processes.

The phase contribution results indicate that fillers influence the system mainly by modifying the balance between early brownmillerite reaction and later C_2S hydration. Because later-age strength in these systems is expected to depend strongly on the extent of C_2S reaction and the formation of binding hydrates, the higher C_2S contribution observed at 56 days, particularly in quartz-containing samples, suggests a greater potential for continued strength development. This interpretation is consistent with the compressive strength measurement previously observed for these systems [17], where the addition of filler systematically increased the strength of citrate- activated BOF slag samples (Appendix B, Figure B1). In contrast, the earlier increase of C_2S contribution in limestone-containing samples is consistent with faster formation of hydration products and earlier microstructural densification [17], which may also contribute to strength development.

3.4.3. *Hydration product proportions*

Fig. 10 shows the total amount of hydration products in all samples at 7 and 56 days, together with the crystalline and amorphous phases detected in the pastes. Hydrogarnets are the dominant hydration products in all systems, mainly as crystalline katoite detected by XRD, while the mass-balance model also indicates the presence of katoite and hibschite in the amorphous fraction. Overall, hydrogarnets represent at least 50% of the total hydration products in all samples.

A small amount of crystalline pyroaurite is detected by XRD at early age but tends to disappear with time. Mass-balance calculations nevertheless indicate that a residual quantity persists over time, therefore assumed to be in a poorly crystalline form [39]. This interpretation is consistent with the continued presence at 56 days of elements such as

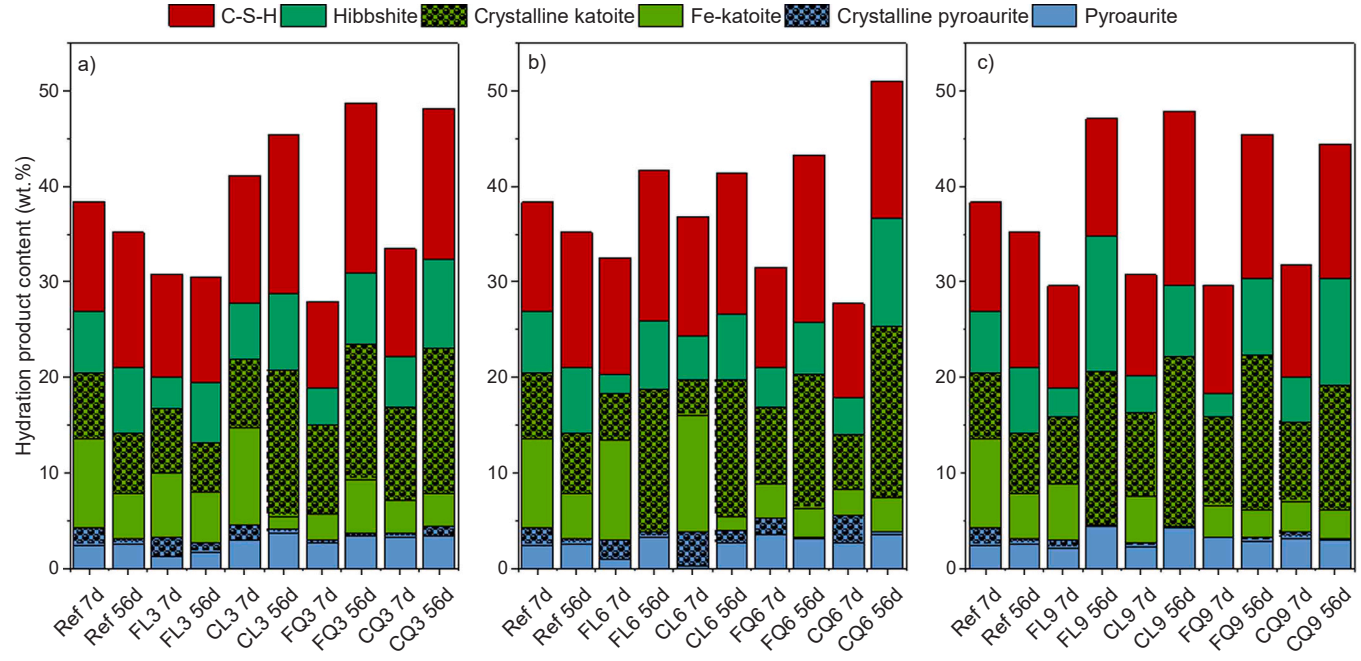

Fig. 10. Measured crystalline hydration products (XRD) and composition of the amorphous hydration products modelled based on PARC phase elemental compositions (a) 3% of filler; b) 6% of filler; c) 9% of filler).

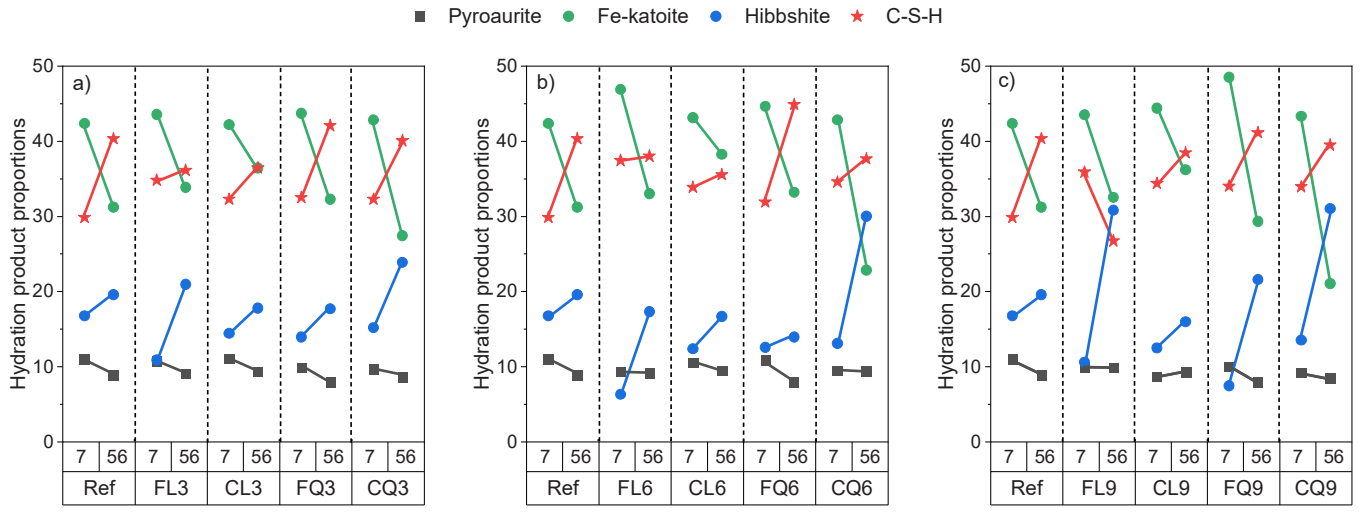

Fig. 11. Evolution of the amorphous hydration product proportion based on PARC phase elemental compositions (a) 3% of filler; b) 6% of filler; c) 9% of filler).

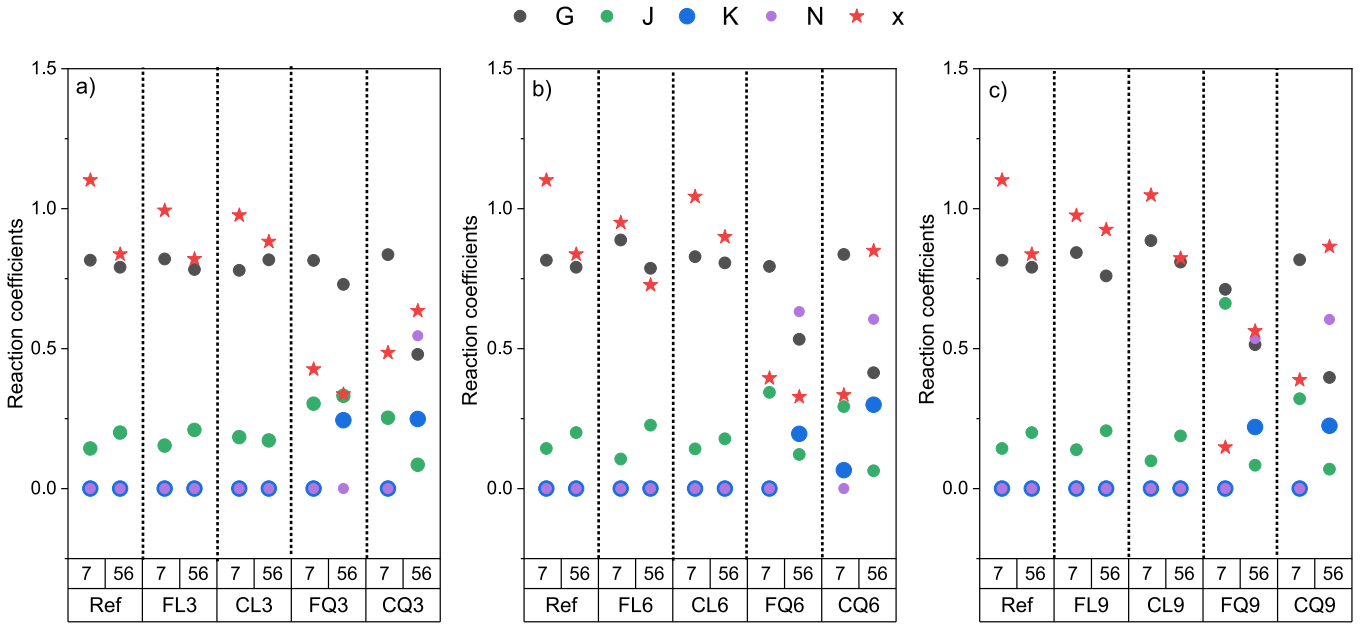

Fig. 12. Coefficient of the reactions describing BOF slag hydration, G accounts for hydrogarnet + C-S-H formation, J for pyroaurite, K for C-S-H formed from C2S hydration, N for wuestite oxidation and x represents the amount of Si in hydrogarnets, (a) 3% fille r; b) 6% of filler; c) 9% of filler).

Mg, Mn and Fe, which are incorporated into pyroaurite in the mass-balance calculation [10,39].

Fig. 11 highlights the relative proportions of the amorphous hydration products. At 7 days, katoite dominates in all samples, consistent with the rapid hydration of brownmillerite. At 56 days, however, C-S-H becomes the dominant product in most systems, often accompanied by an increase in hibschite. This indicates that the slower hydration of C_2S becomes more significant after the early reaction stage, supplying additional silica that contributes both to C-S-H formation and to the enrichment of hydrogarnets in silica, modifying the katoite/hibschite ratio over time. This evolution can be related to changes in solution chemistry during hydration. The rapid dissolution of brownmillerite at early age favours the formation of Fe-rich hydrogarnets such as katoite. As hydration progresses, the increasing contribution of C_2S dissolution provides additional silica to the pore solution, which promotes the formation of more silica-rich hydrogarnets such as hibschite and the precipitation of C-S-H. The progressive shift in the katoite/hibschite balance therefore reflects both the change in the dominant reacting phase and the resulting evolution of Ca and Si availability in the system. However, as previously mentioned, because the model used fixed representative compositions for katoite, hibschite and C-S-H, part of the variation in the calculated proportions may reflect compositional changes within the hydrates rather than strictly changes in their absolute abundance.

The influence of filler type becomes clearer at later ages. Limestone-containing samples show hydrate assemblages very similar to the reference, indicating mainly an increase in the overall amount of hydration products. In contrast, quartz-containing samples show a stronger shift in hydrate composition, with increased hibschite and C-S-H and reduced katoite. This behaviour is consistent with the enhanced contribution of C_2S hydration previously observed in quartz systems.

3.4.4. Overall reactions occurring in citrate activated BOF Slag system with fine fillers

Fig. 12 presents the coefficients of the four reactions used to describe BOF slag hydration. The reaction associated with coefficient G,

corresponding to hydrogarnet formation from brownmillerite and C_2S, clearly dominates the hydration process and accounts for approximately 70–80% of the total reaction. The silica content of the hydrogarnets is represented by parameter x, which reflects the distribution of silica between hydrogarnets and C-S-H. The second reaction (J) corresponds to pyroaurite formation from brownmillerite and wuestite and represents approximately 15–30% of the total reaction. Because some variability in the reaction coefficients can be observed between samples, the corresponding LSQ residuals are reported in Appendix C Table C3 to provide an indication of the fit quality. These values range between 0 and 1.3 across all samples and curing ages, indicating that the observed variations in the coefficients reflect differences between systems rather than numerical instability of the fitting procedure. The reaction coefficients show very similar behaviour between the reference system and limestone-containing mixtures, confirming that limestone mainly acts as a physical filler in the present system. No carboaluminate hydrates were detected, unlike in Portland cement systems where limestone reacts with aluminates. This difference likely results from the relatively low aluminium content of the BOF slag used in this study. In contrast, quartz-containing samples show a higher contribution of the reaction associated with C_2S hydration (K), confirming that quartz promotes the hydration of C_2S. From a macroscopic perspective, the higher contribution of the C_2S hydration reaction (K) in quartz-containing mixtures is consistent with the increased formation of C-S-H observed in Section 3.4.4, which is expected to contribute to the improved compressive strength reported for filler-containing BOF slag systems (Appendix B Figure B1) [17]. This effect is most likely related to the nucleation effect of quartz particles, which provide additional surfaces for C-S-H precipitation. Differences in particle morphology and surface area between quartz and limestone fillers may also influence hydrate nucleation and growth, further contributing to the different hydration behaviour observed between the two filler types [40,41].

3.4.5. *Volatile content in hydration products and model limitations*

The reliability of the mass balance model was evaluated by comparing the predicted amounts of H_2O and CO_2 associated with the calculated hydration products with the experimental mass losses measured by TGA (Fig. 13). The predicted H_2O contents range from 2 to 6 wt%, while predicted CO_2 contents range from 0.05 to 0.2 wt%. Experimentally, the mass losses in the 40–540 °C and 600–800 °C ranges are between 5 and 8 wt% and 0–1.3 wt%, respectively. In most cases, the calculated values underestimate the measured ones.

To better understand the origin of these discrepancies, a two-way ANOVA was performed to evaluate the influence of sample age, filler nature, filler size and filler dosage on the difference between the measured and calculated volatile contents.

For H_2O, the analysis indicates that filler nature ($p = 0.013$) and filler dosage ($p = 0.087$) have a noticeable influence on the deviation between measured and calculated values, while the influence of age remains weaker. For CO_2, the most influential parameters are sample age ($p = 0.01$) and filler nature ($p = 0.02$), as well as their interaction ($p = 0.045$).

BOF slag systems are known to be sensitive to carbonation [42], particularly at longer curing times. This likely explains the higher CO_2 contents measured experimentally. For example, the measured CO_2 content in the reference sample increases from 0.25 wt% at 7 days to approximately 1 wt% at 56 days, while the calculated value remains nearly constant. In addition, fillers may influence carbonation behaviour. Both limestone and quartz particles can act as nucleation sites for $CaCO_3$ precipitation [21,22,42,43], which may explain the higher CO_2 contents measured in filler-containing samples. This effect is particularly visible at 7 days, where samples containing fillers show higher

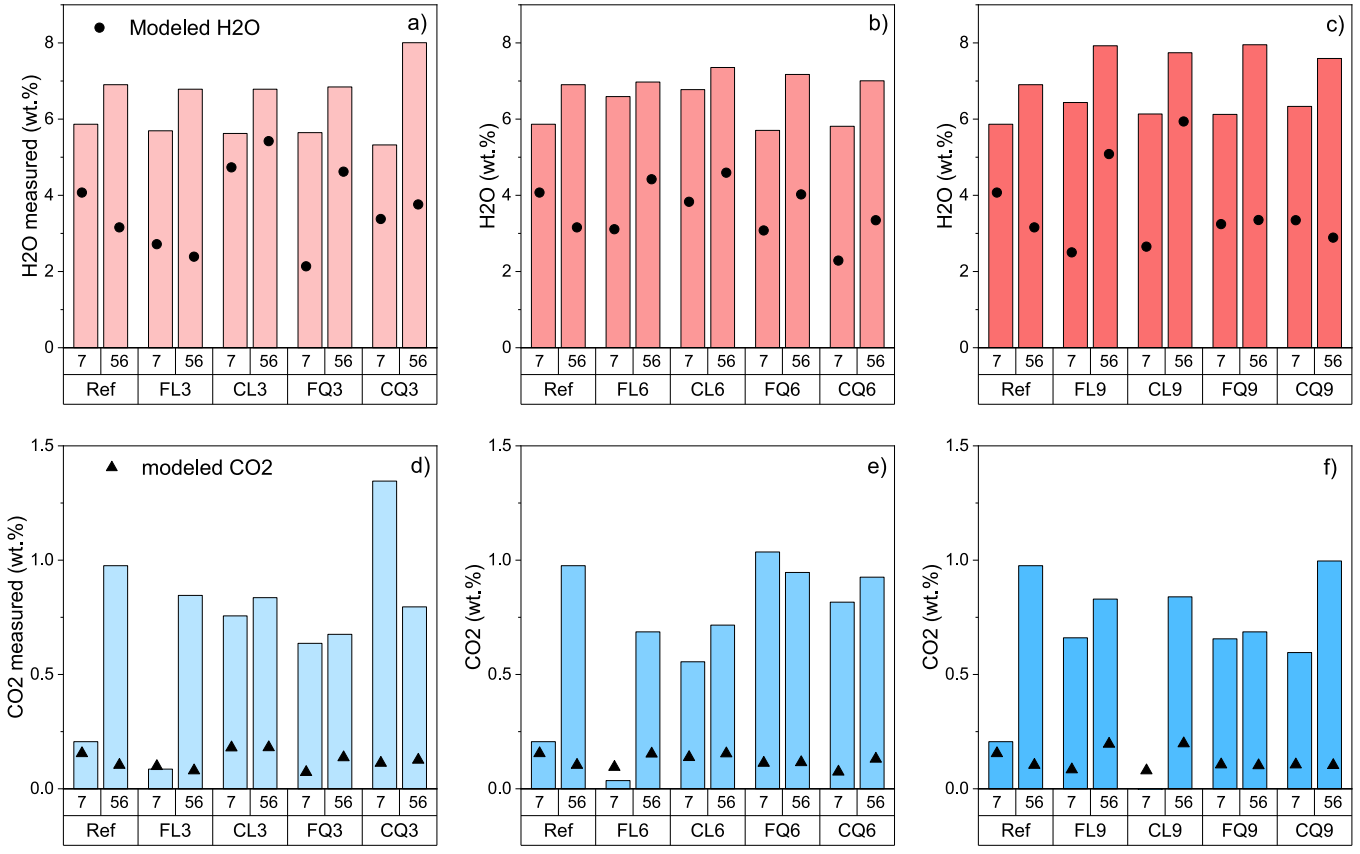

Fig. 13. Volatile compounds measured versus modelled in the BOF slag paste samples. The columns represent the values determined with TGA and the dots correspond to the calculated values, (a), b), c) bound H_2O in the samples containing 3, 6 and 9% of filler; d), e), f) CO_2 in the samples containing 3, 6 and 9% of filler).

measured CO_2 contents than the reference system while calculated values remain similar.

The discrepancy observed for H_2O may also be related to the simplifying assumptions used in the mass balance model. In the model, hydration products are represented using fixed stoichiometric compositions, implying a fixed water content. Phases such as C-S-H can accommodate variable amounts of bound water, depending on parameters such as reaction age, filler presence and Ca/Si ratio. Hydrogarnets may evolve from Fe-rich compositions (katoite) toward more silica-rich compositions (hibschite) as additional silica becomes available in the system. Because the model constrains these phases to fixed compositions, part of the chemical variability of the system is absorbed through adjustments in the relative proportions of the modelled phases. Consequently, the calculated phase proportions should be interpreted as best-fit estimates that reproduce the overall chemical balance of the system, rather than exact quantitative measurements of the real hydrate contents. Similarly, although the correction applied for fine filler particles reduces the direct influence of undetected filler on the hydration product composition, small residual contributions cannot be completely excluded and may contribute to the remaining variability.

Despite these limitations, the model successfully captures the relative trends between systems and curing ages. The interpretation therefore focuses primarily on comparisons and reaction trends rather than exact quantitative amounts of individual hydration products, which limits the sensitivity of the conclusions to the modelling assumptions.

4. Conclusion

The study assessed the phase assemblage of BOF slag hydrated pastes activated with tri-potassium citrate and compared the influence of quartz and limestone filler on the phase reactivity, the chemical composition of the hydration products, the contribution of the reactive phase in the reaction and the proportions the different hydration product. Analysis such quantitative XRD, SEM-EDX combined with PARC and mass balance calculation were performed and helped to find the following conclusions:

- Reactive phases: Brownmillerite (C_2F) and belite (C_2S) are the main contributors to BOF slag hydration, while wuestite and magnetite contribute only marginally.
- Evolution over time: At 7 days, C_2F and C_2S contribute in similar proportions, but at 56 days C_2S becomes dominant, enriching hydrates in silica.
- Effect of fillers: Limestone mainly accelerates early hydration without major changes in hydrate proportions, while quartz enhances C_2S reactivity at later ages, increasing C–S–H and hibschite contents.
- Hydration products: Hydrogarnets remain the main products (>50% of total hydrates), with katoite prevailing at early ages and hibschite and C–S–H increasing over time. Pyroaurite persists as a minor but stable phase (<10%).
- Model assessment: The mass balance model reproduces the main hydration trends but underestimates volatile contents, mainly due to carbonation and the assumption of fixed hydrate compositions.

Overall, the results confirm that BOF slag hydration in citrate-activated systems is mainly governed by the reactivity of brownmillerite and C_2S. The presence of fillers modifies the relative contribution of these phases and the resulting hydrate assemblage, but the main hydration mechanisms remain the same. Limestone mainly increases the overall amount of hydration products without strongly altering their proportions, whereas quartz promotes a higher contribution of C_2S and shifts the hydrate assemblage toward more silica-rich phases. The model provides a consistent framework to describe these reactions, although some deviations highlight the influence of carbonation and a possible variability in hydration product composition.

CRediT authorship contribution statement

T. Wattez: Writing – review & editing, Supervision, Resources. **K. Schollbach:** Supervision, Software, Conceptualization. **H.J.H. Brouwers:** Writing – review & editing, Supervision, Project administration, Funding acquisition. **S. Van der Laan:** Writing – review & editing, Supervision, Software, Resources, Methodology, Conceptualization. **Yvars S:** Writing – original draft, Methodology, Investigation.

Declaration of Competing Interest

The authors declare that they have no known competing financial interests or personal relationships that could have appeared to influence the work reported in this paper.

Acknowledgement

The authors would like to express their gratitude to Ecocem (Grant ID: RT103465) for sponsoring this research. Additionally, the authors would like to acknowledge Tata Steel IJmuiden for providing the raw materials and for conducting the quantitative XRD and the SEM/PARC measurements.

Appendix A. Supporting information

Supplementary data associated with this article can be found in the online version at doi:10.1016/j.conbuildmat.2026.146271.

Data availability

Data will be made available on request.

References

[1] IPCC, *Climate Change 2022 - Mitigation of Climate Change - Full Report*, no. 1. 2022.
[2] C. Shi, Steel Slag—Its Production, Processing, Characteristics, and Cementitious Properties, J. Mater. Civ. Eng. 16 (3) (2004) 230–236, https://doi.org/10.1061/(asce)0899-1561(2004)16:3(230).
[3] D. Ph, "Steel Slag: Chemistry, Mineralogy, and Morphology," pp. 2816–2825, 2015.
[4] T.S. Naidu, C.M. Sheridan, L.D. van Dyk, Basic oxygen furnace slag: review of current and potential uses (p), Min. Eng. 149 (January) (2020) 106234, https://doi.org/10.1016/j.mineng.2020.106234.
[5] S. Mishra, Characteristics and applications of basic oxygen furnace slag as a sustainable construction material—A review, Int. J. Pavement Res. Technol. (0123456789) (2025), https://doi.org/10.1007/s42947-025-00528-1.
[6] S.Z. Carvalho, F. Vernilli, B. Almeida, M. Demarco, S.N. Silva, The recycling effect of BOF slag in the portland cement properties, Resour. Conserv. Recycl. 127 (September) (2017) 216–220, https://doi.org/10.1016/j.resconrec.2017.08.021.
[7] A.M. Kaja, K. Schollbach, S. Melzer, S.R. van der Laan, H.J.H. Brouwers, Q. Yu, Hydration of potassium citrate-activated BOF slag (p), Cem. Concr. Res. 140 (ember 2020) (2021) 106291, https://doi.org/10.1016/j.cemconres.2020.106291.
[8] A.M. Kaja, A. Delsing, S.R. van der Laan, H.J.H. Brouwers, Q. Yu, Effects of carbonation on the retention of heavy metals in chemically activated BOF slag pastes (p), Cem. Concr. Res 148 (ember 2020) (2021) 106534, https://doi.org/10.1016/j.cemconres.2021.106534.
[9] A.M. Kaja, S. Melzer, H.J.H. Brouwers, Q. Yu, On the optimization of BOF slag hydration kinetics (p), Cem. Concr. Compos. 124 (January) (2021) 104262, https://doi.org/10.1016/j.cemconcomp.2021.104262.
[10] W.F. Santos, K. Schollbach, S. Melzer, S.R. van der Laan, H.J.H. Brouwers, Quantitative analysis and phase assemblage of basic oxygen furnace slag hydration (p), J. Hazard Mater. 450 (February) (2023) 131029, https://doi.org/10.1016/j.jhazmat.2023.131029.
[11] W. Franco Santos, J.J. Botterweg, S. Chaves Figueiredo, K. Schollbach, S. van der Laan, H.J.H. Brouwers, Sodium oxalate activation of basic oxygen furnace slag for building materials (p), Resour. Conserv. Recycl. 198 (January) (2023) 107174, https://doi.org/10.1016/j.resconrec.2023.107174.
[12] J.C.O. Zepper, S.R. van der Laan, K. Schollbach, H.J.H. Brouwers, A Bogue approach applied to basic oxygen furnace slag (p), Cem. Concr. Res. 175 (October 2023) (2024) 107344, https://doi.org/10.1016/j.cemconres.2023.107344.
[13] J.C.O. Zepper, S.R. van der Laan, K. Schollbach, H.J.H. Brouwers, Reactivity of BOF slag under autoclaving conditions (p), Constr. Build. Mater. 364 (December 2022) (2023) 129957, https://doi.org/10.1016/j.conbuildmat.2022.129957.
[14] Y. Jiang, T.C. Ling, C. Shi, S.Y. Pan, Characteristics of steel slags and their use in cement and concrete—A review, Elsevier B.V, Sep. 01, 2018, https://doi.org/10.1016/j.resconrec.2018.04.023.

[15] J.C.O. Zepper, S. de Bruin, X. Ling, K. Schollbach, S.R. van der Laan, H.J. H. Brouwers, Improving the early reactivity of activated basic oxygen furnace slag – The influence of particle fineness and grinding aids, J. CO2 Util. 83 (2024) (2024) 102821, https://doi.org/10.1016/j.jcou.2024.102821.
[16] Y. Tang, K. Schollbach, S. van der Laan, W. Chen, Activation of BOF slag with dipotassium hydrogen phosphate: Enhancing hydration, carbonation resistance, and heavy metal leaching (p), Cem. Concr. Compos 157 (December 2024) (2025) 105922, https://doi.org/10.1016/j.cemconcomp.2025.105922.
[17] S. Yvars, K. Schollbach, T. Wattez, S. Van Der Laan, H.J.H. Brouwers, Influence of limestone filler on potassium citrate activated BOF slag binder (p), Constr. Build. Mater. 494 (October 2024) (2025) 143424, https://doi.org/10.1016/j.conbuildmat.2025.143424.
[18] J. Péra, S. Husson, B. Guilhot, Influence of finely ground limestone on cement hydration, Cem. Concr. Compos. 21 (2) (1999) 99–105, https://doi.org/10.1016/S0958-9465(98)00020-1.
[19] Y. Briki, M. Zajac, M.Ben Haha, K. Scrivener, Impact of limestone fineness on cement hydration at early age, Cem. Concr. Res. 147 (Sep. 2021) 106515, https://doi.org/10.1016/J.CEMCONRES.2021.106515.
[20] B. Lothenbach, G. Le Saout, E. Gallucci, K. Scrivener, Influence of limestone on the hydration of Portland cements, Cem. Concr. Res 38 (6) (2008) 848–860, https://doi.org/10.1016/j.cemconres.2008.01.002.
[21] M. Zajac, A. Rossberg, G. Le Saout, B. Lothenbach, Influence of limestone and anhydrite on the hydration of Portland cements, Cem. Concr. Compos. 46 (Feb. 2014) 99–108, https://doi.org/10.1016/J.CEMCONCOMP.2013.11.007.
[22] S.H. Kang, Y. Jeong, K.H. Tan, J. Moon, The use of limestone to replace physical filler of quartz powder in UHPFRC, Cem. Concr. Compos 94 (April) (2018) 238–247, https://doi.org/10.1016/j.cemconcomp.2018.09.013.
[23] E. Berodier, K. Scrivener, Understanding the filler effect on the nucleation and growth of C-S-H, J. Am. Ceram. Soc. 97 (12) (2014) 3764–3773, https://doi.org/10.1111/jace.13177.
[24] K. Scrivener, R. Snellings, B. Lothenbach. A Practical Guide to Microstructural Analysis of Cementitious Materials, 2018, 10.1201/b19074.
[25] C. van Hoek, J. Small, S. van der Laan, Large-Area Phase Mapping Using PhAse Recognition and Characterization (PARC) Software, Micros. Today 24 (5) (2016) 12–21, https://doi.org/10.1017/s1551929516000572.
[26] K. Schollbach, M.J. Ahmed, S.R. Laan, The mineralogy of air granulated converter slag, Int. J. Ceram. Eng. Sci. 3 (1) (2021) 21–36, https://doi.org/10.1002/ces2.10074.
[27] K. Schollbach, S. van der Laan, Microstructure analysis with quantitative phase mapping using SEM-EDS and Phase Recognition and Characterization (PARC) Software, Appl. Steelmak. slag (2022), https://doi.org/10.1515/9783110674941-003.
[28] "Synthesis and characterization of hydrogarnet Ca3(AlxFe1−x)2(SiO4)y(OH)4 (3−y) | Elsevier Enhanced Reader", Accessed: Oct. 05, 2021. [Online]. Available: ⟨https://reader.elsevier.com/reader/sd/pii/S000888461400043X?token=212679933C1F457133D345D509F85BF406454664E2E6279900E9AAB3A24E436F9E7AF4E7537EDBA25DB27982056510D1&originRegion=eu-west-1&originCreation=20211005111017⟩.
[29] D. Wang, et al., Cement and Concrete Research Hydrotalcite-pyroaurite solid solution in cement system: Molecular structure and thermodynamic properties (p), Cem. Concr. Res. 197 (June) (2025) 107976, https://doi.org/10.1016/j.cemconres.2025.107976.
[30] E. Tajuelo Rodriguez, K. Garbev, D. Merz, L. Black, I.G. Richardson, Thermal stability of C-S-H phases and applicability of Richardson and Groves' and Richardson C-(A)-S-H(I) models to synthetic C-S-H, Cem. Concr. Res. 93 (2017) 45–56, https://doi.org/10.1016/j.cemconres.2016.12.005.
[31] S.J. Palmer, H.J. Spratt, R.L. Frost, Thermal decomposition of hydrotalcites with variable cationic ratios, J. Therm. Anal. Calor. 95 (1) (2009) 123–129, https://doi.org/10.1007/s10973-008-8992-4.
[32] J. Siramanont, B.J. Walder, L. Emsley, P. Bowen, Iron incorporation in synthetic precipitated calcium silicate hydrates, Cem. Concr. Res. 142 (2021) 106365, https://doi.org/10.1016/j.cemconres.2021.106365.
[33] Y.F. Chen, et al., Room temperature syntheses and thermal behaviors of hydrogarnets Sr3M2(OH)12 (M = Al, Cr and Fe), J. Alloy. Compd. 637 (2015) 248–252, https://doi.org/10.1016/j.jallcom.2015.02.215.
[34] K.S.P. Karunadasa, C.H. Manoratne, H.M.T.G.A. Pitawala, R.M.G. Rajapakse, Thermal decomposition of calcium carbonate (calcite polymorph) as examined by in-situ high-temperature X-ray powder diffraction, J. Phys. Chem. Solids 134 (January) (2019) 21–28, https://doi.org/10.1016/j.jpcs.2019.05.023.
[35] T. Chen, X. Zhu, Y. Li, Y. Han, Thermal decomposition kinetics of limestone with different particle sizes in an air atmosphere (p.), J. Taiwan Inst. Chem. Eng. 176 (May) (2025) 106292, https://doi.org/10.1016/j.jtice.2025.106292.
[36] J.M. Jones, L.I. Darvell, T.G. Bridgeman, M. Pourkashanian, A. Williams, An investigation of the thermal and catalytic behaviour of potassium in biomass combustion (II), Proc. Combust. Inst. 31 (2) (2007) 1955–1963, https://doi.org/10.1016/j.proci.2006.07.093.
[37] A. Marcilla, A. Gómez-Siurana, M. Beltrán, I. Martínez-Castellanos, I. Blasco, D. Berenguer, TGA/FTIR study of the behavior of sodium and potassium citrates in the decomposition of 3R4F tobacco. N2 and air atmospheres, Thermochim. Acta 657 (September) (2017) 31–38, https://doi.org/10.1016/j.tca.2017.09.017.
[38] P.C. Hewlett, "Lea's Chemistry of Cement and Concrete,", Lea'S. Chem. Cem. Concr. (2003) 1–1057, https://doi.org/10.1016/B978-0-7506-6256-7.X5007-3.
[39] K. Rozov, et al., Synthesis and characterization of the LDH hydrotalcite-pyroaurite solid-solution series, Cem. Concr. Res. 40 (8) (2010) 1248–1254, https://doi.org/10.1016/j.cemconres.2009.08.031.
[40] I. Soroka, N. Stern, Calcareous fillers and the compressive strength of portland cement, Cem. Concr. Res. 6 (3) (1976) 367–376, https://doi.org/10.1016/0008-8846(76)90099-5.
[41] T. Oey, A. Kumar, J.W. Bullard, N. Neithalath, G. Sant, The filler effect: The influence of filler content and surface area on cementitious reaction rates, J. Am. Ceram. Soc. 96 (6) (2013) 1978–1990, https://doi.org/10.1111/jace.12264.
[42] A.M. Kaja, A. Delsing, S.R. van der Laan, H.J.H. Brouwers, Q. Yu, Effects of carbonation on the retention of heavy metals in chemically activated BOF slag pastes (p), Cem. Concr. Res. 148 (June) (2021) 106534, https://doi.org/10.1016/j.cemconres.2021.106534.
[43] D.P. Bentz, E.F. Irassar, B.E. Bucher, W.J. Weiss, Limestone Fillers Conserve Cement - Part 1: An analysis based on Powers' model, Concr. Int. 3 (ember) (2009) 41–46. ⟨http://concrete.nist.gov/~bentz/ci3111bentzreadonly.pdf⟩.